



Construction of hierarchical and self-supported NiFe-Pt₃Ir electrode for hydrogen production with industrial current density

Zhenrui Ni ^a, Cheng Luo ^a, Bei Cheng ^a, Panyong Kuang ^{b,*}, Youji Li ^c, Jiaguo Yu ^{b,*}

^a State Key Laboratory of Advanced Technology for Materials Synthesis and Processing, Wuhan University of Technology, 122 Luoshi Road, Wuhan 430070, PR China

^b Laboratory of Solar Fuel, Faculty of Materials Science and Chemistry, China University of Geosciences, 388 Lumo Road, Wuhan 430074, PR China

^c College of Chemistry and Chemical engineering, Jishou University, Jishou 416000, PR China



ARTICLE INFO

Keywords:

Self-supported electrode
NiFe nanosheets
Pt₃Ir alloy nanoparticles
Hydrogen evolution reaction
Industrial current densities

ABSTRACT

Rational design and fabrication of electrocatalysts from the perspective of mass transfer and electronic structure is highly desirable for hydrogen evolution reaction (HER). Herein, a hierarchical and self-supported electrode comprising Cu nanowires, NiFe nanosheets, and Pt₃Ir alloy nanoparticles (Cu NWs@NiFe-Pt₃Ir) was in situ constructed and established as a highly active and robust electrocatalyst for HER with industrial current densities. Benefiting from the hierarchical structure, abundant active sites, and positive electronic interaction between NiFe and Pt₃Ir, the Cu NWs@NiFe-Pt₃Ir electrode shows extremely low overpotentials of 210 and 239 mV to reach industrial current densities of 500 and 1000 mA cm⁻² in 1.0 M KOH solution, respectively. More importantly, Cu NWs@NiFe-Pt₃Ir electrode shows robust durability with a slight increment of 8 mV for the required potential after consecutive tests for 7 days under 500 mA cm⁻². As further revealed by electrochemical and theoretical studies, the reaction kinetics of NiFe is greatly promoted by coupling with Pt₃Ir, and the d-band center energy level of Pt 5d orbital is lowered by Ir atom, which not only facilitates the electron consumption at the electrode/electrolyte interface but also optimizes the energies for H adsorption and H₂ desorption. This work provides valuable insights into the construction of self-supported electrodes with extraordinary activity and durability for industrial applications.

1. Introduction

Nowadays, energy crises and environmental issues are the most severe threats facing human beings. The development of clean and renewable alternatives to fossil fuels has become a top priority [1–5]. In recent years, hydrogen (H₂) has received extensive research interest due to its merits of cleanliness, renewability, and high energy density [6–12]. Among diverse technologies for H₂ production, hydrogen evolution reaction (HER) from electrochemical water splitting has shown great promise in high-purity H₂ production under industrial conditions [13–16]. Although plenty of electrocatalysts have been fabricated and investigated for high-current-density HER, the trade-off between overall performance and economic cost still has room to maneuver [17–19].

Electrode usually plays a significant role in determining the catalytic activity [20–24]. Compared with binder-involved electrodes, in situ constructed self-supported electrodes based on popular current collectors, such as Cu foam, Ni foam, and Ni mesh, are even more attractive for high current density investigations due to their extraordinary electron

transfer capability and excellent durability [25–29]. Such current collectors could provide large interior surface areas for nanomaterials growing, including nanowires (NWs), nanosheets (NSs), and nanoparticles (NPs), endowing self-supported electrodes with abundant active sites for catalytic reactions [30–35]. Moreover, the three-dimensional (3D) and hierarchical framework of self-supported electrodes are believed to provide efficient triphase reaction areas for electron diversion, ion transport, and gaseous product diffusion, which are highly conducive to exhibiting low overpotential and robust long-term stability under industrial current densities [36–39]. For example, Feng et al. developed a self-supported electrode composed of Ni foam and Co@FeOOH core-shell nanotube arrays [40]. By taking advantage of the high electrical conductivity of Ni foam and unobstructed mass transfer channels in Co@FeOOH nanotube arrays, the as-prepared electrode exhibits a competitive overpotential of 385 mV to reach a current density of 300 mA cm⁻² for oxygen evolution reaction (OER) and shows excellent long-term stability under a constant current density of 200 mA cm⁻² for 50 h. Using Ni foam as a support, B-doped

* Corresponding authors.

E-mail addresses: kuangpanyong@cug.edu.cn (P. Kuang), yujiaguo93@cug.edu.cn (J. Yu).

NiCo LDH-decorated Ni foam (B-NiCo LDH/NF) electrode was constructed via facile strategies by Yang et al. [41]. Attributed to abundant active sites and enhanced mass transfer ability, B-NiCo LDH/NF electrode shows low overpotentials of 286 and 381 mV at industrial current densities of 500 and 1000 mA cm⁻² for HER, respectively. Besides, Yu et al. prepared a self-supported electrode (Cu@NiFe LDH) composed of NiFe LDH, Cu NWs, and Cu foam. Benefiting from the large surface area and promoted spatial mass transfer ability, Cu@NiFe LDH electrode achieves an industrial current density of 1000 mA cm⁻² at an extremely low overpotential of 315 mV for OER [42]. Based on foregoing discussions, self-supported electrodes could achieve low overpotential and exceptional durability at industrial current densities and are expected to trigger rapid advances in the development of high-performance energy conversion and storage devices.

In addition to fast electron delivery in current collectors, rapid transfer and consumption of electrons at the electrode/electrolyte interface are also indispensable for obtaining industrial current densities at low overpotentials. Taking the extensively studied NiFe LDH as an example, bare NiFe LDH-based electrode usually exhibits unsatisfactory HER activities even though the advantages of current collectors are fully utilized, due to the limited mass transfer and sluggish reaction kinetics caused by the poor electrical conductivity of NiFe LDH [43,44]. Encouragingly, coupling with bimetallic alloy is recently found to be an effective strategy to promote HER activities of NiFe LDH [45–47]. Attributed to the intimate contact between NiFe LDH and bimetallic alloy, electrons delivered from current collectors can be rapidly injected into alloy and then consumed by reduction reaction in time. Besides, electronic structure optimization usually happens between two metal components in bimetallic alloy, leading to the favorable electron redistribution effect and strengthened metal–H bond, which could significantly improve the H₂ evolution rate at the electrode/electrolyte interface. For example, Cai et al. reported the modulation of *d*-band center (ε_d) of Ru 4d_z² orbital and the precise regulation of Ru–H interaction by incorporating Ni and Co metals, thus resulting in superior HER activity [48]. Wang et al. observed that the introduction of Cu makes a downward shift of the ε_d in NiCu and balances the energies for H adsorption and H₂ desorption, thus resulting in greatly improved HER activities [49].

Inspired by former studies, herein, we fabricated the Cu NWs@NiFe-LDH (Cu NWs@NiFe) core@shell structure supported on Cu foam and followed by electro-deposition of Pt₃Ir alloy NPs (Cu NWs@NiFe-Pt₃Ir). The in situ grown Cu NWs with unique forest-like structure provide not only fast channels for electron transfer but also considerable platforms for NiFe NSs decoration. Moreover, the surface of 2D NiFe NSs is loaded with Pt₃Ir alloy NPs with an average diameter of 8 nm, which contact NiFe closely and function a positive role in consuming electrons via the electrode/electrolyte interface. As a result, the hierarchical Cu NWs@NiFe-Pt₃Ir electrode exhibits extremely low overpotentials (η_{500} and η_{1000}) of 210 and 239 mV to reach industrial current densities of 500 and 1000 mA cm⁻² for HER in 1.0 M KOH solution, respectively, much comparable to the majority of the state-of-the-art electrodes reported. Moreover, Cu NWs@NiFe-Pt₃Ir electrode shows an inappreciable rise of 8 mV in the applied potential after consecutive operation for 7 days under an industrial current density of 500 mA cm⁻², demonstrating its great promise in practical applications. Electrochemical and theoretical studies prove that the reaction kinetics of NiFe is greatly promoted by coupling with Pt₃Ir alloy NPs, which facilitates the electron consumption at the electrode/electrolyte interface. More importantly, electronic structure modulation of Pt 5d orbital by Ir atom is further revealed, in where Ir reduces the ε_d energy level of Pt 5d orbital and optimizes both the adsorption and desorption energies of H and H₂, thus resulting in improved HER activity. This work provides constructive insights into the design and fabrication of self-supported electrodes with outstanding activity and durability under industrial conditions.

2. Experimental section

2.1. Materials and chemicals

Cu foam (thickness: 1.5 mm), hydrochloric acid (HCl), ammonium persulfate [(NH₄)₂S₂O₈], sodium hydroxide (NaOH), potassium bicarbonate (KHCO₃), iron(II) sulfate heptahydrate (FeSO₄·7 H₂O), nickel(II) nitrate hexahydrate (Ni(NO₃)₂·6 H₂O), potassium hydroxide (KOH), chloroplatinic acid hexahydrate (H₂PtCl₆·6 H₂O), and ethanol (C₂H₆O) were purchased from Sinopharm Chemical Reagent Co., Ltd. IrCl₃ was purchased from Shanghai Macklin Biochemical Co., Ltd.

2.2. Preparation of Cu NWs

Cu NWs were synthesized via the chemical oxidation method. Firstly, a piece of Cu foam (1 cm × 2.5 cm) was immersed into the HCl (10 wt%) aqueous solution for 10 min and then washed adequately with distilled water. Then, the pre-clean Cu foam was immersed into a mixture solution (70 mL) containing 2 g of (NH₄)₂S₂O₈ and 7 g of NaOH for 25 min. By conducting the chemical oxidation process, Cu foam covered by vertically aligned Cu(OH)₂ NWs was obtained. Finally, Cu NWs can be prepared by calcination of Cu(OH)₂ NWs in the air (180 °C, 30 min) to form CuO NWs and followed by the electrochemical reduction of CuO NWs in N₂ purged KHCO₃ solution (−0.4 V vs. reversible hydrogen electrode (RHE), 4000 s).

2.3. Fabrication of Cu NWs@NiFe

Cu NWs@NiFe was synthesized through an electro-deposition strategy. Cu NWs, Pt slice, and saturated calomel electrode (SCE) were used as the working electrode, counter electrode, and reference electrode, respectively. The electro-deposition process was conducted in an N₂-saturated solution composed of 0.15 M Ni(NO₃)₂·6 H₂O and 0.15 M FeSO₄·7 H₂O for 30 s with an applied potential of −1.0 V vs. SCE.

2.4. Fabrication of Cu NWs@NiFe-Pt₃Ir

Cu NWs@NiFe-Pt₃Ir was fabricated by an electro-deposition method. Cu NWs@NiFe, graphite rod, and SCE were performed as the working electrode, counter electrode, and reference electrode, respectively. The electro-deposition process was carried out by performing cyclic voltammetry (CV) cycles in a 1.0 M KOH aqueous solution containing 225 μM H₂PtCl₆ and 25 μM IrCl₃ for 300 segments with a scan rate of 50 mV s⁻¹. The applied potential region of CV cycle ranges from −1.068 to −1.568 V vs. SCE. Analogously, counterparts of Cu NWs@NiFe-Pt and Cu NWs@NiFe-Ir were also prepared by the same synthetic routes, except that H₂PtCl₆ and IrCl₃ were added into 1.0 M KOH solution alone, respectively.

3. Results and discussion

3.1. Synthesis and characterizations

The synthetic route of Cu NWs@NiFe core@shell architecture is illustrated in Fig. 1a. Specifically, one piece of pre-clean Cu foam was immersed into a mixture solution of NaOH and (NH₄)₂S₂O₈ with an optimal time of 25 min (Fig. S1) and served as the platform for Cu(OH)₂ NWs in situ growing through a chemical oxidation process (Fig. 1b and Fig. S2a-b). Cu NWs were then prepared by calcination of the Cu(OH)₂ NWs under the atmosphere to form CuO NWs and followed by the electrochemical reduction treatment (Fig. 1c and Fig. S2c-d). Finally, using the Cu NWs-decorated Cu foam as a cathode, an electro-deposition strategy was adopted to fabricate the Cu NWs@NiFe core@shell structure (Fig. 1d). Note that the forest-like array structure of Cu NWs is well maintained even after the destructive calcination and reduction treatments, revealing its robust structural stability. Moreover, the vertically

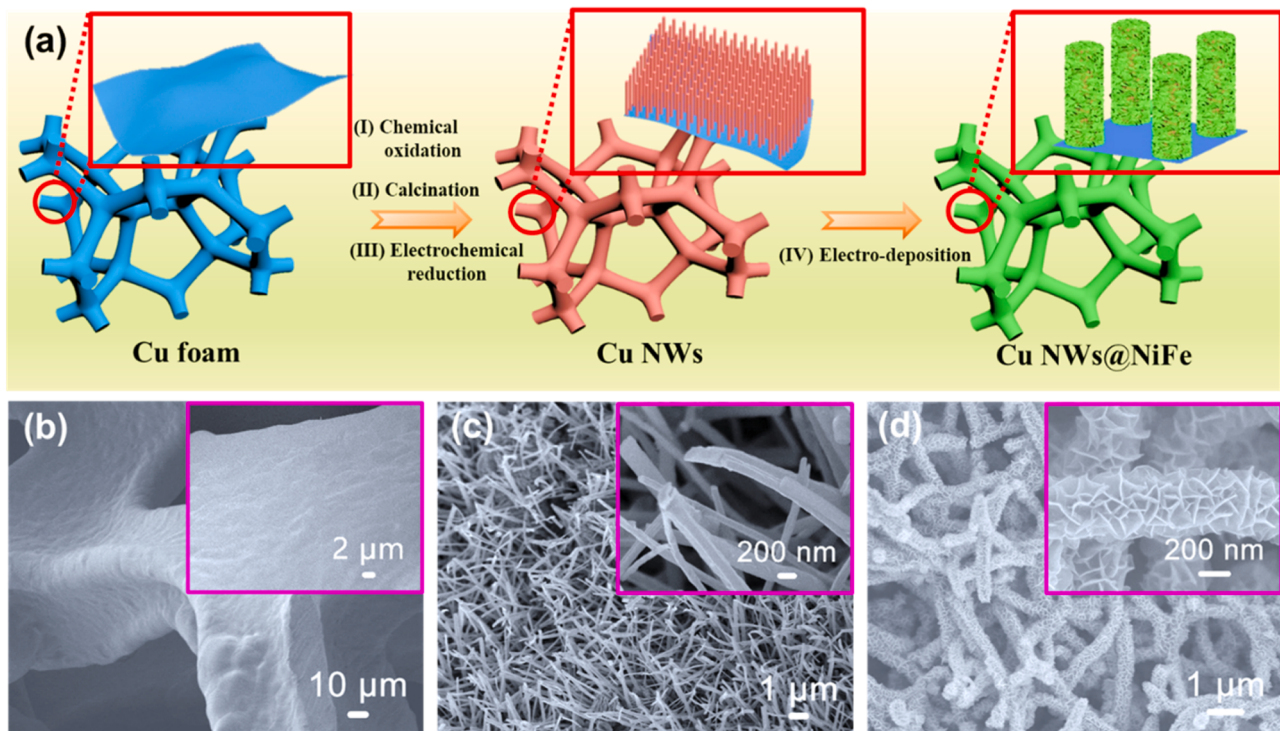


Fig. 1. (a) Schematic illustration for the synthetic process of Cu NWs@NiFe. Step I: Chemical oxidation of Cu foam to form Cu(OH)₂ NWs. Step II: Calcination of Cu(OH)₂ NWs to form CuO NWs. Step III: Electrochemical reduction of CuO NWs to form Cu NWs. Step IV: Electro-deposition of NiFe NSs on Cu NWs to fabricate Cu NWs@NiFe. SEM images of the (b) Cu foam, (c) Cu NWs, and (d) Cu NWs@NiFe.

aligned NiFe NSs on Cu NWs provide not only large surface area for Pt₃Ir alloy NPs depositing but also sufficient spaces and channels for mass transfer. Fig. S3 displays digital photos of the prepared samples with varied colors, suggesting the successful preparation of Cu NWs@NiFe. In addition, NiFe NSs-covered Cu foam was also synthesized by the same strategy, and SEM images reveal the uniform distribution of NiFe NSs on Cu foam (Fig. S4).

Employing the as-prepared Cu NWs@NiFe as a support, Pt₃Ir alloy NPs were further deposited via a facile electro-deposition method. As can be seen from SEM images in Fig. 2a-b, Cu NWs@NiFe-Pt₃Ir shows the same hierarchical structure as Cu NWs@NiFe, and Pt₃Ir alloy NPs are evenly distributed on the surface of NiFe NSs. Fig. 2c displays the core@shell structure of Cu NWs@NiFe-Pt₃Ir, in which the black part in the middle, the thin slices in the outer region, and the randomly distributed dark spots correspond to the Cu NWs core, NiFe NSs shell, and Pt₃Ir alloy NPs, respectively. Moreover, no severely aggregated NPs are observed, suggesting the vital role of 2D NiFe NSs in distributing Pt₃Ir alloy NPs. Fig. 2d presents the high-resolution TEM (HRTEM) image of the NiFe-Pt₃Ir part. Pt₃Ir alloy NPs possess an average diameter of 8 nm, which contact with the NiFe NSs closely. The intimate contact between NiFe and Pt₃Ir is believed to promote electron transfer and reaction kinetics. The inset of Fig. 2d displays a lattice finger of 0.22 nm, ascribing to the (111) plane of Pt₃Ir alloy. Furthermore, energy-dispersive X-ray (EDX) elemental mapping images in Fig. 2e-h exhibit the accurate distribution of Pt and Ir elements over Pt₃Ir alloy NPs. Fig. 2i shows the uniform distribution of Ni, Fe, Pt, and Ir elements on Cu NWs, further verifying the successful fabrication of Cu NWs@NiFe-Pt₃Ir. X-ray diffraction (XRD) patterns in Fig. S5 display three intensive characteristic diffraction peaks located at around 44, 51, and 74°, corresponding to the (111), (200), and (220) planes of face-centered cubic (fcc) Cu (PDF# 04-0836). Compared with bare Cu NWs, a broad and weak diffraction peak in both Cu NWs@NiFe and Cu NWs@NiFe-Pt₃Ir is attributed to the amorphous phase of NiFe. However, due to the strong diffraction peaks of Cu and low content of Pt₃Ir, characteristic

diffraction peaks of Pt₃Ir alloy cannot be detected. The relative contents of Pt and Ir are determined by inductively coupled plasma-optical emission spectrometry (ICP-OES) measurement. As shown in Table S1, the molar ratio of Pt:Ir is calculated to be 3:1, suggesting the formation of Pt₃Ir alloy. For comparison, counterparts of Cu NWs@NiFe supported Pt and Ir NPs (denoted as Cu NWs@NiFe-Pt and Cu NWs@NiFe-Ir) were also prepared and their corresponding microstructural information is presented in Figs. S6–8, respectively.

Surface chemical states of the Cu NWs@NiFe-Pt₃Ir were investigated by X-ray photoelectron spectroscopy (XPS) measurements. XPS survey spectrum in Fig. 3a shows the co-existence of Cu, Ni, Fe, Pt, and Ir elements in Cu NWs@NiFe-Pt₃Ir. Fig. 3b presents the Cu 2p XPS spectrum, in which two peaks with binding energies of 934.7 and 954.1 eV are ascribed to the Cu 2p_{3/2} and Cu 2p_{1/2}, and two satellite peaks are located at 942.7 and 962.6 eV, respectively. Additionally, two peaks centered at 932.5 and 952.4 eV correspond to the metallic state of Cu⁰ originating from Cu NWs or Cu foam [50]. Fig. 3c-d display the Ni 2p and Fe 2p XPS spectra, respectively. Two peaks with binding energies of 856.1 and 873.4 eV in Ni 2p XPS spectrum can be assigned to the species of Ni 2p_{3/2} and Ni 2p_{1/2}, along with two satellite peaks with binding energies of 861.9 and 879.6 eV, respectively (Fig. 3c) [51,52]. For Fe 2p XPS spectrum, two prominent peaks located at 712.2 and 722.9 eV are attributed to the Fe 2p_{3/2} and Fe 2p_{1/2}, together with two satellite peaks with binding energies of 717.8 and 731.4 eV, respectively (Fig. 3d) [53–55]. Pt 4f XPS spectrum in Fig. 3e can be deconvoluted into two kinds of Pt species. Specifically, two peaks located at binding energies of 71.1 and 74.3 eV are ascribed to the 4f_{7/2} and 4f_{5/2} of Pt(II) species, while two peaks located at 72.9 and 75.8 eV are attributed to the 4f_{7/2} and 4f_{5/2} of Pt(IV) species, respectively [56,57]. Moreover, several peaks associated with Cu 3p and its related satellite peak contribute to the wide and intensive peak in Pt 4f XPS spectrum. As for Ir 4f XPS spectrum, two fitted peaks located at binding energies of 60.5 and 63.4 eV are ascribed to the Ir 4f_{7/2} and Ir 4f_{5/2} of Ir(0) species, while two peaks with binding energies of 62.4 and 65.4 eV are attributed to

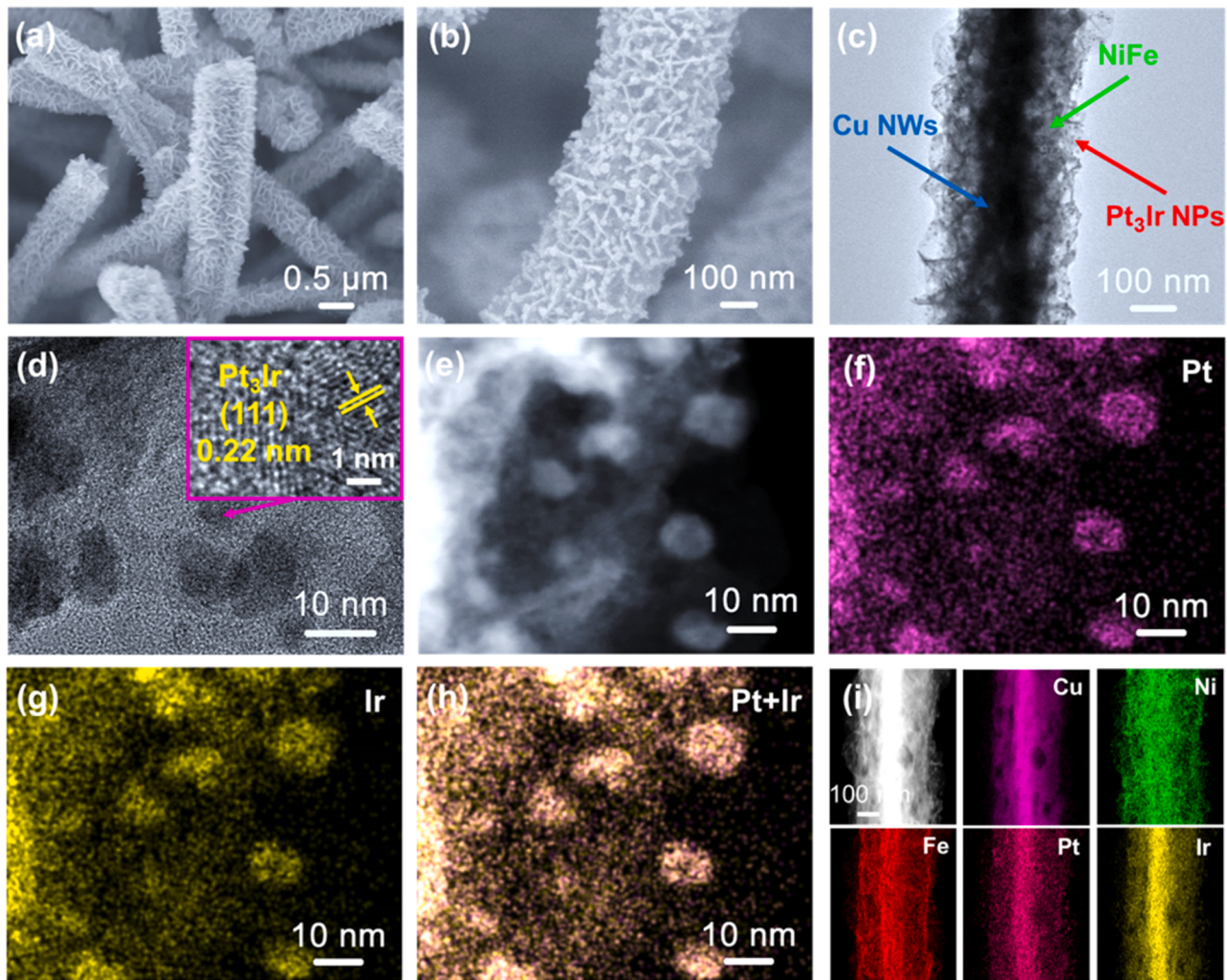


Fig. 2. (a-b) SEM, (c) TEM, (d) HRTEM, and (e-i) EDX elemental mapping images of the Cu NWs@NiFe-Pt₃Ir. The inset of (d) shows the lattice finger of one representative Pt₃Ir alloy NP.

the Ir 4 f_{7/2} and Ir 4 f_{5/2} of Ir(IV) species, respectively (Fig. 3f).

3.2. Performance evaluation

HER activity of the Cu NWs@NiFe-Pt₃Ir was assessed using a standard three-electrode system in 1.0 M KOH solution. Compared to bare Cu foam, Cu NWs shows improved HER activity due to its unique forest-like architecture that promotes electron transfer and mass transport (Fig. S9). Additionally, HER activities of Cu NWs@NiFe-Pt_xIr samples with varied concentration ratios of Pt:Ir were initially evaluated. As shown in Fig. S10, Cu NWs@NiFe-Pt_xIr with a concentration ratio of 9:1 for Pt:Ir (Pt:Ir molar ratio is 3:1), i.e. Cu NWs@NiFe-Pt₃Ir, shows the best HER activity with a lowest η_{500} value of 210 mV. Further performance evaluations and theoretical studies were therefore carried out with Cu NWs@NiFe-Pt₃Ir sample. Fig. 4a exhibits linear sweep voltammetry (LSV) curves of the Cu NWs@NiFe-Pt₃Ir, Cu NWs@NiFe-Pt, Cu NWs@NiFe-Ir, Cu NWs@NiFe, Cu NWs, and Pt wire. Dramatically, HER activity of Cu NWs@NiFe was significantly improved after introducing Pt₃Ir alloy NPs. As displayed in Fig. 4b, Cu NWs@NiFe-Pt₃Ir shows extremely low η_{500} and η_{1000} values of 210 and 239 mV, respectively, much lower than those of the Cu NWs@NiFe-Pt ($\eta_{500} = 309$ mV, $\eta_{1000} = 382$ mV), Cu NWs@NiFe-Ir ($\eta_{500} = 391$ mV, $\eta_{1000} = 442$ mV), Cu NWs@NiFe ($\eta_{500} = 427$ mV, $\eta_{1000} = 487$ mV), and Pt wire ($\eta_{500} = 307$ mV, $\eta_{1000} = 380$ mV). Moreover, the superior HER activity of Cu NWs@NiFe-Pt₃Ir is significantly comparable to some previously

reported state-of-the-art electrodes, such as Ni_{2(1-x)}Mo_{2x}P ($\eta_{500} = 240$ mV, $\eta_{1000} = 294$ mV) [58], Ni₂P/NF ($\eta_{500} = 242$ mV, $\eta_{1000} = 306$ mV) [34], V-Ni₅P₄ ($\eta_{500} = 243$ mV, $\eta_{1000} = 295$ mV) [59], IrNi₂-FeNi₃/NF ($\eta_{500} = 249$ mV, $\eta_{1000} = 289$ mV) [60], 2 H Nb_{1.35}S₂ ($\eta_{500} = 275$ mV, $\eta_{1000} = 370$ mV) [61], F₂P-Fe₃O₄/IF ($\eta_{500} = 278$ mV, $\eta_{1000} = 321$ mV) [62], LiCoBPO/NF ($\eta_{500} = 370$ mV, $\eta_{1000} = 391$ mV) [63], Pd₄S/Pd₃P_{0.95} ($\eta_{500} = 387$ mV, $\eta_{1000} = 486$ mV) [64], and HC-MoS₂/Mo₂C ($\eta_{500} = 400$ mV, $\eta_{1000} = 441$ mV) [65] (Fig. 4c and Table S2), revealing the strong competitiveness of Cu NWs@NiFe-Pt₃Ir toward industrial applications.

Ascribed to the collaborative effect of forest-like Cu NWs and the intimate contact between NiFe NSs and Pt₃Ir alloy NPs, both electron transfer in the bulk phase and mass transport at the electrode/electrolyte interface are greatly promoted in Cu NWs@NiFe-Pt₃Ir. As proved by recorded Nyquist plots at different η values in Fig. 4d and Fig. S11. Cu NWs@NiFe-Pt₃Ir possesses the smallest series resistance ($R_s \approx 2.5 \Omega$) in comparison with other counterparts ($R_s \approx 2.7 \sim 3.2 \Omega$). Moreover, Cu NWs@NiFe-Pt₃Ir shows a much smaller semicircle than other samples in low-frequency regions, indicating the decreased interfacial mass transport resistance. In other words, Pt₃Ir alloy NPs greatly promote the electron migration and reactant delivery at the electrode/electrolyte interface, thereby dramatically improving the reaction kinetics. Bode plots further corroborate the significant role of Pt₃Ir alloy NPs in facilitating the mass transport at the electrode/electrolyte interface (Fig. S11). Each peak of the plots corresponds to a typical control process

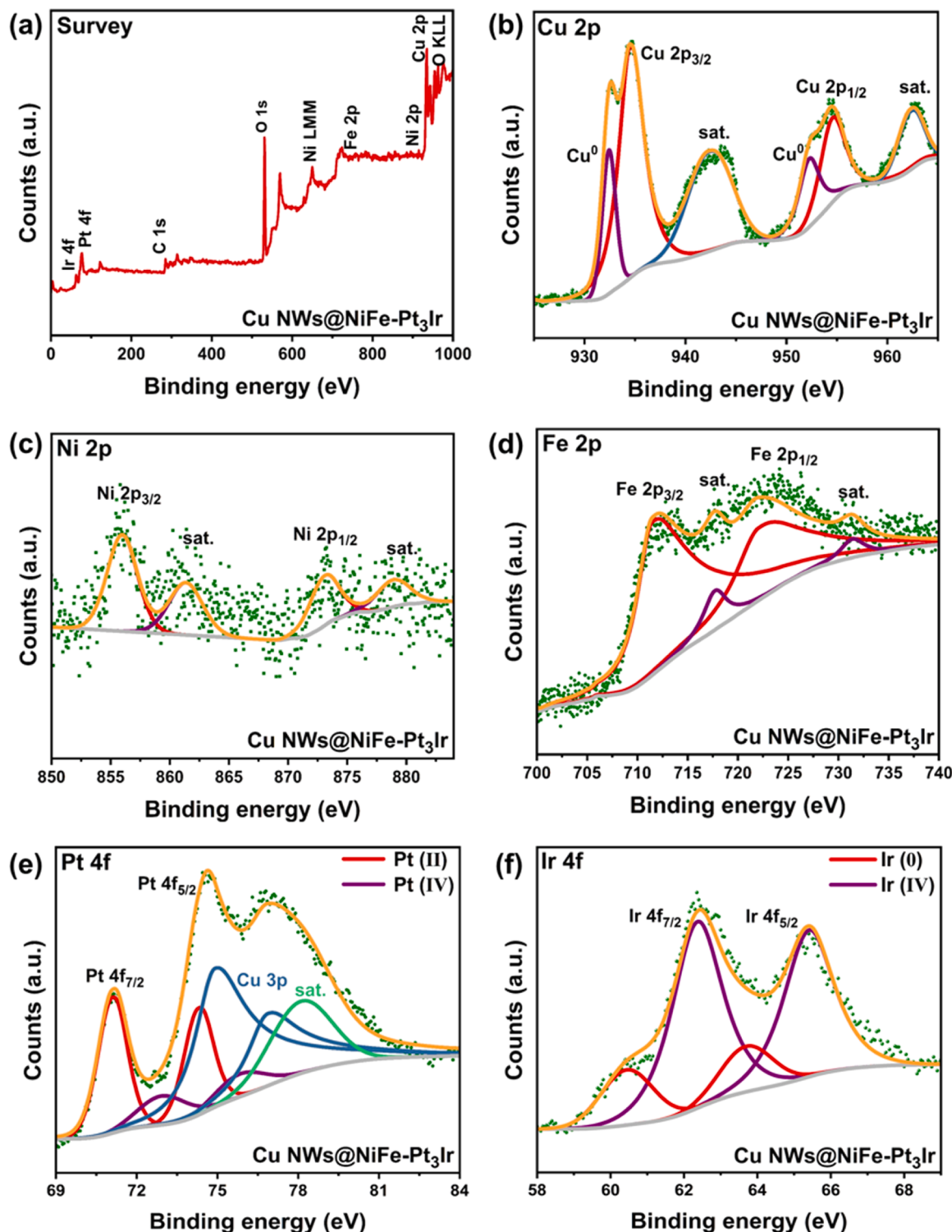


Fig. 3. (a) XPS survey spectrum, (b) Cu 2p XPS spectrum, (c) Ni 2p XPS spectrum, (d) Fe 2p XPS spectrum, (e) Pt 4f XPS spectrum, and (f) Ir 4f XPS spectrum of the Cu NWs@NiFe-Pt₃Ir.

of the reaction in an electrode, and the higher the peak, the more dominant control of the corresponding process [66,67]. It can be seen that all samples exhibit higher peaks in low-frequency regions at varied η values, suggesting the decisive step of mass transport at the electrode/electrolyte interface, which in turn highlights the importance of introduced Pt₃Ir alloy NPs to promote the reaction kinetics of Cu NWs@NiFe-Pt₃Ir. Additionally, cyclic voltammetry (CV) measurements were performed to estimate the electrochemical active surface area

(ECSA) of samples. As presented in Fig. 4e and Fig. S12, Cu NWs@NiFe-Pt₃Ir possesses an ECSA value of 62.7 mF cm^{-2} , which is 1.3, 1.5, 2.1, and 3.5 times larger than that of the Cu NWs@NiFe-Pt (46.7 mF cm^{-2}), Cu NWs@NiFe-Ir (41.9 mF cm^{-2}), Cu NWs@NiFe-LDH (30.3 mF cm^{-2}), and Cu NWs (17.9 mF cm^{-2}), respectively, implying a much larger accessible electrochemical surface area and more exposed active sites for H₂ evolution after the decoration of Pt₃Ir alloy NPs.

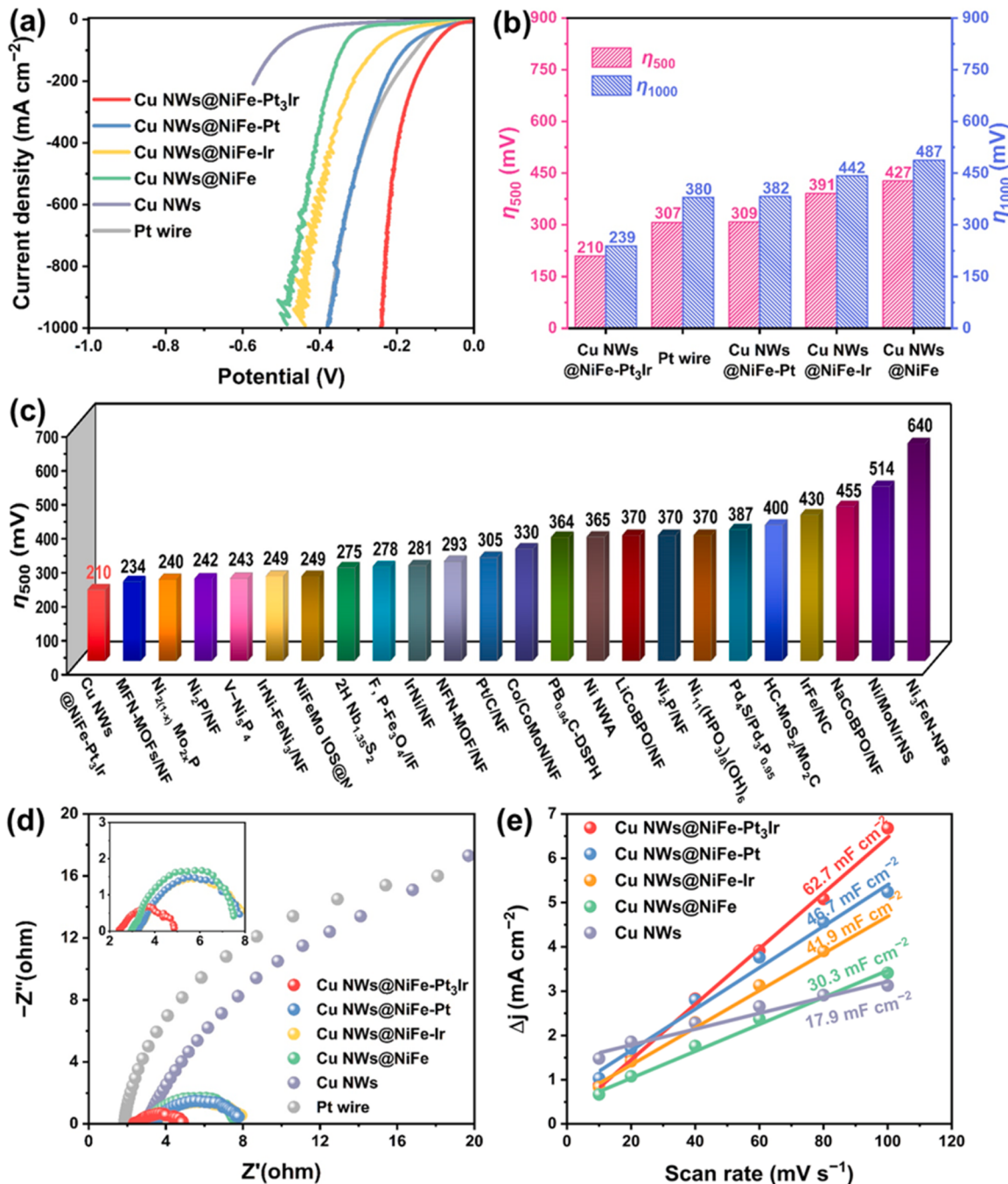


Fig. 4. (a) LSV curves and (b) η_{500} and η_{1000} values of the Cu NWs@NiFe-Pt₃Ir, Cu NWs@NiFe-Pt, Cu NWs@NiFe-Ir, Cu NWs@NiFe, Cu NWs, and Pt wire, respectively. (c) Comparison of η_{500} values between Cu NWs@NiFe-Pt₃Ir and other previously reported HER electrodes. (d) Nyquist plots of the Cu NWs@NiFe-Pt₃Ir, Cu NWs@NiFe-Pt, Cu NWs@NiFe-Ir, Cu NWs@NiFe, Cu NWs, and Pt wire. (e) ECSA values of the Cu NWs@NiFe-Pt₃Ir, Cu NWs@NiFe-Pt, Cu NWs@NiFe-Ir, Cu NWs@NiFe, and Cu NWs.

3.3. Stability test and characterization

For practical applications, competitive electrodes should exhibit not only high current densities at low η values but also extraordinary durability under industrial current densities. Therefore, the long-term stability of Cu NWs@NiFe-Pt₃Ir was evaluated by a chronopotentiometry test under industrial current density. As shown in Fig. 5a and Video S1, there is a negligible increment (8 mV) in the applied potential to retain the current density of 500 mA cm^{-2} after the consecutive tests for 7 days, indicating the excellent durability of Cu NWs@NiFe-Pt₃Ir. Small fluctuations of the applied potential during

operation are caused by the addition of electrolyte, which is consumed quickly under industrial current density and needs to be replenished in time. The chronopotentiometry curve can therefore more intuitively reflect the excellent stability of Cu NWs@NiFe-Pt₃Ir. Contrarily, applied potentials of Cu NWs@NiFe-Pt, Cu NWs@NiFe-Ir, and Cu NWs@NiFe significantly increased after long-term stability tests, suggesting that the synergistic effect of NiFe NSs and Pt₃Ir alloy NPs is essential to facilitate the mass transport and realize the robust stability. In addition, as indicated by LSV curves and Nyquist plots shown in Fig. 5b, η_{100} , η_{500} , and η_{1000} values as well as the mass transfer ability of Cu NWs@NiFe-Pt₃Ir remain almost the same after the long-term stability test.

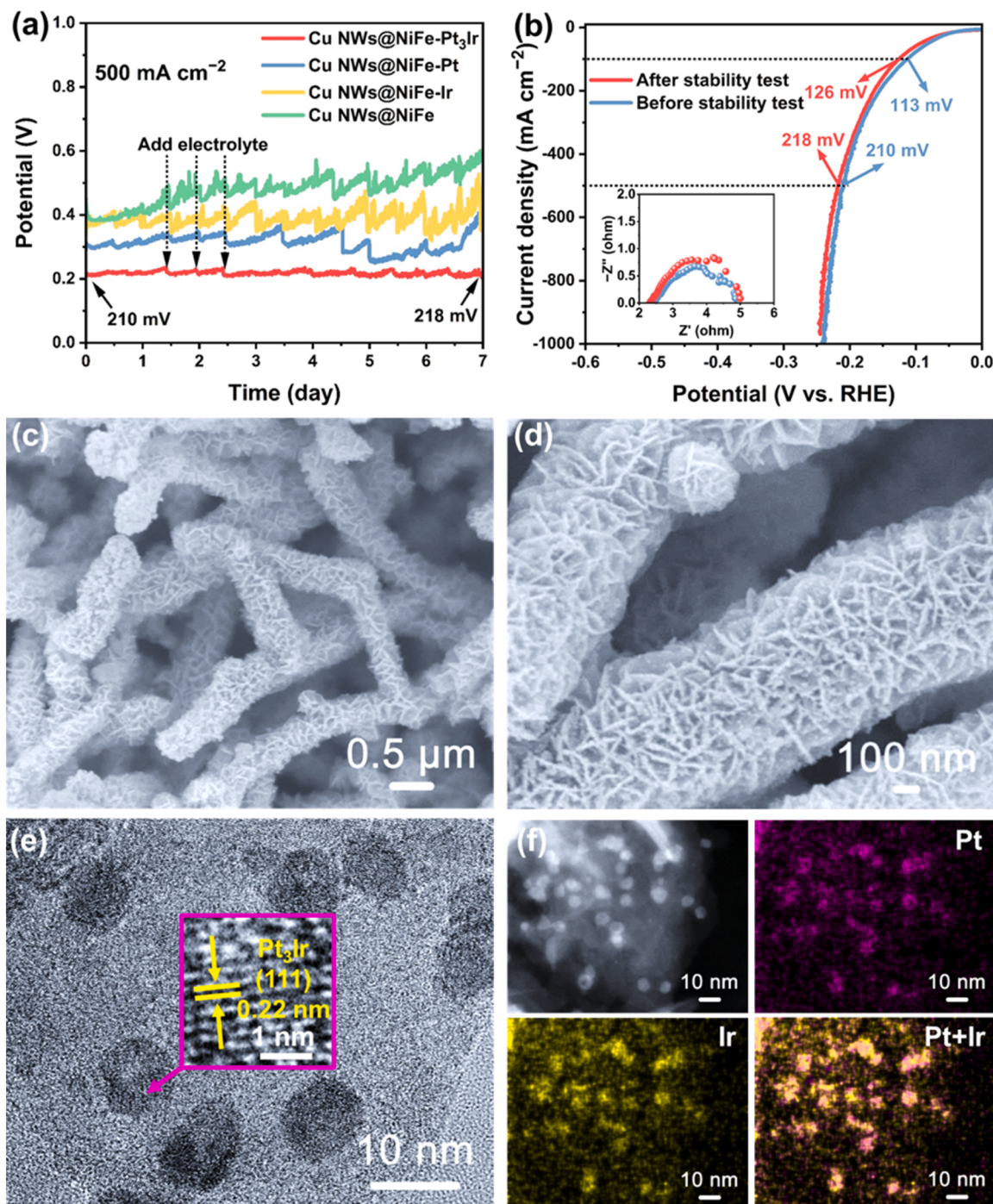


Fig. 5. (a) Chronopotentiometry curves of the Cu NWs@NiFe-Pt₃Ir, Cu NWs@NiFe-Pt, Cu NWs@NiFe-Ir, and Cu NWs@NiFe. (b) LSV curves and Nyquist plots of the Cu NWs@NiFe-Pt₃Ir before and after the long-term stability test. (c-d) SEM, (e) HRTEM, and (f) EDX elemental mapping images of the Cu NWs@NiFe-Pt₃Ir after a long-term stability test.

Supplementary material related to this article can be found online at doi:10.1016/j.apcatb.2022.122072.

The preceding electrochemical measurements disclose the superb reaction kinetics and durability of Cu NWs@NiFe-Pt₃Ir to achieve industrial current density under alkaline conditions. Microstructural information and chemical composition of Cu NWs@NiFe-Pt₃Ir after long-term stability test were further investigated. Fig. 5c-e display the SEM and HRTEM images of Cu NWs@NiFe-Pt₃Ir after the long-term stability test, in which the hierarchical structure is well preserved and Pt₃Ir alloy NPs are still evenly distributed on the surface of NiFe NSs. Moreover, EDX elemental mapping images reveal the homogeneous distribution of

Pt and Ir elements over Pt₃Ir alloy NPs (Fig. 5f). Furthermore, XRD pattern of the Cu NWs@NiFe-Pt₃Ir after the long-term durability test matches well with that of the initial one, suggesting that there is no phase variation of Cu NWs@NiFe-Pt₃Ir under high-current-density operation (Fig. 6a). Besides, Cu, Ni, Fe, Pt, and Ir elements can be clearly detected for Cu NWs@NiFe-Pt₃Ir before and after the long-term stability test (Fig. 6b). Specifically, peak intensities and binding energies of Ni 2p, Fe 2p, Pt 4f, and Ir 4f XPS spectra after the long-term durability test are almost identical to those of the initial one, strongly indicating that there are no composition and chemical state variations for Cu NWs@NiFe-Pt₃Ir under industrial-current-density operation (Fig. 6c-f).

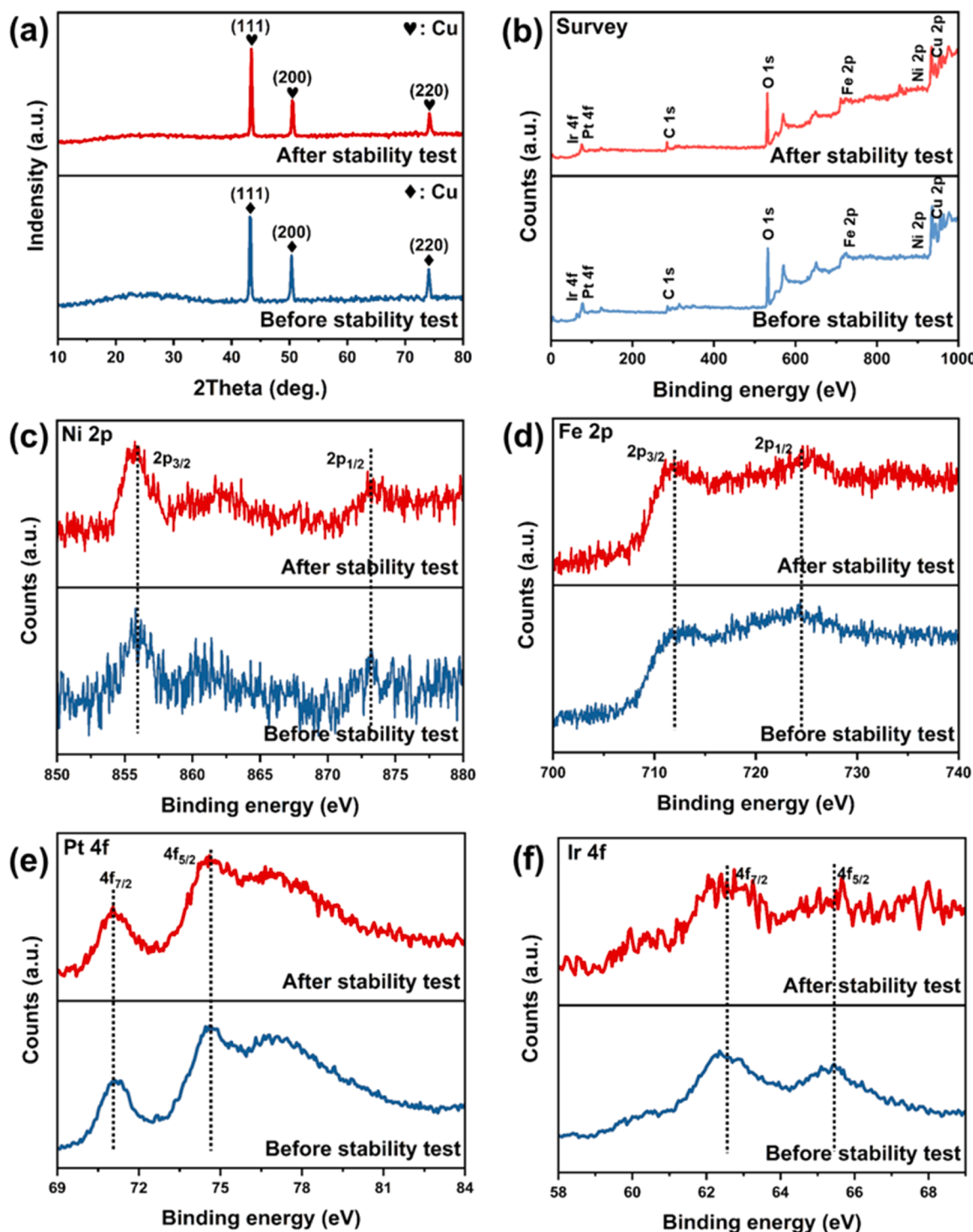


Fig. 6. (a) XRD patterns, (b) XPS survey spectra, (c) Ni 2p XPS spectra, (d) Fe 2p XPS spectra, (e) Pt 4 f XPS spectra, and (f) Ir 4 f XPS spectra of the Cu NWs@NiFe-Pt₃Ir before and after long-term stability test.

3.4. DFT calculations

Density functional theory (DFT) calculations further elaborate the synergistic effect of Pt₃Ir and NiFe in Cu NWs@NiFe-Pt₃Ir and reveal the essential interaction between Pt 5d and H 1s orbitals. For comparison, structure models of Cu NWs@NiFe-Pt₃Ir, Cu NWs@NiFe-Pt, and Cu NWs@NiFe-Ir were constructed (Fig. 7a and Figs. S13 and 14). As shown in Fig. 7b and Figs. S15–17, Cu NWs@NiFe-Pt₃Ir (H adsorbed on Pt atom), Cu NWs@NiFe-Pt₃Ir (H adsorbed on Ir atom), Cu NWs@NiFe-Pt,

Cu NWs@NiFe-Ir, and Cu NWs@NiFe exhibit Gibbs free energy of H adsorption (ΔG_{H^*}) values of -0.31 , 0.57 , -0.43 , -0.97 , and 1.04 eV, respectively. The positive ΔG_{H^*} value of Cu NWs@NiFe-Pt₃Ir (H adsorbed on Ir atom) suggests the weak adsorption of H on the Ir site, which inevitably restricts the HER process. Moreover, the lowest $|\Delta G_{\text{H}^*}|$ value of Cu NWs@NiFe-Pt₃Ir (H adsorbed on Pt atom) indicates the superior HER activity when Pt atoms act as active sites for H₂ generation. The charge density difference ($\Delta\rho$) reveals the strong electronic interaction between NiFe and Pt₃Ir. As shown in Fig. 7c and Fig. S18, electrons are

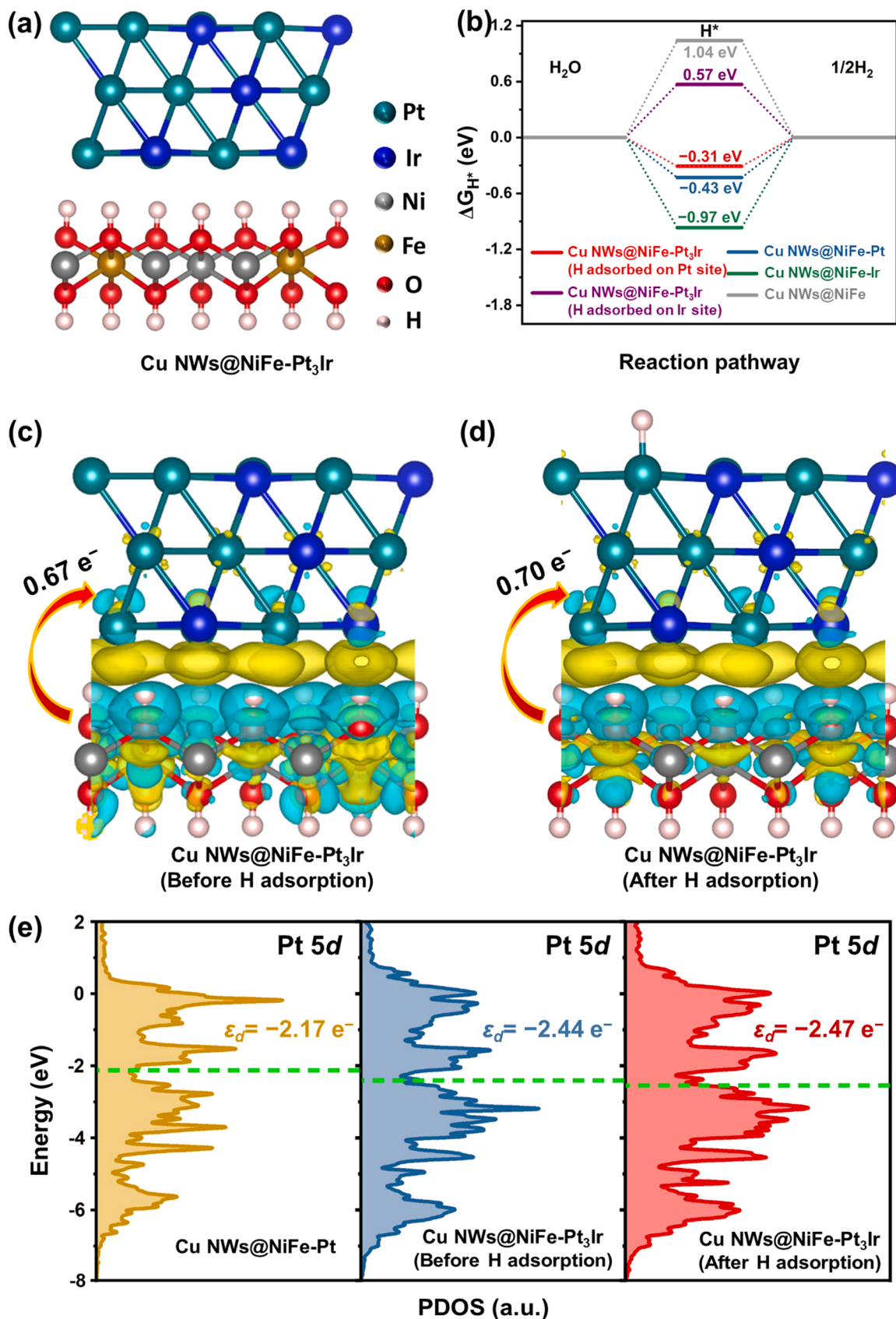


Fig. 7. (a) The atomic structure of Cu NWs@NiFe-Pt₃Ir. (b) Calculated ΔG_{H^*} values of different structures. Changes in the $\Delta\rho$ and the number of transferred electrons in Cu NWs@NiFe-Pt₃Ir (c) before and (d) after H adsorption. (e) Pt 5d orbitals and corresponding ε_d energy levels of the Cu NWs@NiFe-Pt, Cu NWs@NiFe-Pt₃Ir (before H adsorption), and Cu NWs@NiFe-Pt₃Ir (after H adsorption).

accumulated on the marginal region of metal NPs before H adsorption, indicating the electron-donated feature of NiFe and the proton reduction site of metal NPs. Specifically, the numbers of transferred electrons from NiFe to Pt₃Ir, Pt, and Ir are calculated to be 0.67, 0.66, and 0.50 e⁻, respectively, which unambiguously affirms the stronger electronic interaction between NiFe NSs and Pt₃Ir alloy NPs and the relatively stronger ability of Pt₃Ir alloy to reduce the adsorbed proton. More importantly, changes in the $\Delta\rho$ and the number of transferred electrons between NiFe and Pt₃Ir after H adsorption further prove the positive function of Pt₃Ir to facilitate the electron migration via the electrode/electrolyte interface. As shown in Fig. 7d, relatively more electrons are accumulated on the side of Pt₃Ir after H adsorption, and the number of migrated electrons increases from 0.67 to 0.70 e⁻. This accurate variation suggests that more electrons are injected into the active Pt₃Ir alloy after H adsorption and then participate in the proton reduction reaction.

Electronic structures of Pt 5d and H 1s orbitals in Cu NWs@NiFe-Pt₃Ir (H adsorbed on Pt atom) were further analyzed by the projected density of states (PDOS). It is found that the ΔG_{H^*} value and ε_d energy level of Pt₃Ir are precisely modulated by introducing the Ir atom. As shown in Fig. 7e and Fig. S19, Cu NWs@NiFe-Pt₃Ir exhibits a deeper ε_d energy level (-2.44 eV) of Pt 5d orbital compared to that of the Cu NWs@NiFe-Pt (-2.17 eV) while a positively shifted ε_d energy level (-1.73 eV) of Ir 5d orbital in comparison with that of the Cu NWs@NiFe-Ir (-2.20 eV). The deeper the Pt 5d orbital ε_d energy level is, the less $|\Delta G_{\text{H}^*}|$ value it has [49], which is well consistent with the aforementioned description that Cu NWs@NiFe-Pt₃Ir (H adsorbed on Pt atom) possesses the lowest $|\Delta G_{\text{H}^*}|$ value. This result suggests that Ir-incorporation could effectively modulate the ε_d energy level of Pt 5d orbital, thus balancing the adsorption of H and the desorption of H₂. According to the Sabatier principle [68,69], moderate adsorption and desorption energies of the intermediates play a vital role in determining catalytic activities. As a result, with an optimal ΔG_{H^*} value, Cu NWs@NiFe-Pt₃Ir exhibits dramatically reduced η_{500} and η_{1000} values of 210 and 239 mV, respectively, which are much smaller than those of the Cu NWs@NiFe-Pt ($\eta_{500} = 309$ mV, $\eta_{1000} = 382$ mV). In addition, the ε_d energy level of Pt 5d orbital further shifts to a much deeper energy level (-2.47 eV) after its hybridization with the H 1s orbital, suggesting that the adsorbed H could further facilitate the electron transfer and the electronic structure of Pt 5d orbital contributes greatly to the Pt-H interaction. Therefore, from the perspective of ε_d theory, the introduction of Ir lowers the ε_d energy level of Pt 5d orbital and optimizes both the adsorption and desorption energies of H and H₂, thus resulting in promoted HER activity.

4. Conclusions

In summary, a hierarchical and self-supported Cu NWs@NiFe-Pt₃Ir electrocatalyst was in situ constructed and used as a highly active and robust electrode for alkaline HER at industrial current densities. Benefiting from synergistic effects of the unique forest-like structure of Cu NWs, large surface area of NiFe NSs, and uniform distribution of Pt₃Ir alloy NPs, Cu NWs@NiFe-Pt₃Ir electrode exhibits superior activity and robust long-term stability in comparison with other counterparts including Cu NWs@NiFe-Pt, Cu NWs@NiFe-Ir, and Cu NWs@NiFe-Pt₃Ir. Specifically, the as-obtained Cu NWs@NiFe-Pt₃Ir electrode exhibits extremely low η_{500} and η_{1000} values of 210 and 239 mV for HER in 1.0 M KOH solution, respectively. Furthermore, Cu NWs@NiFe-Pt₃Ir electrode shows a negligible increment of 8 mV in the applied potential after consecutive operation for 7 days under an industrial current density of 500 mA cm⁻², revealing its great promise in practical applications. As further proved by electrochemical and theoretical studies, the reaction kinetics of Cu NWs@NiFe is greatly promoted by coupling with Pt₃Ir alloy NPs, which facilitates the electron consumption at the electrode/electrolyte interface and improves the H₂ evolution rate. In addition, the incorporation of Ir atom could precisely modulate the electronic structure of Pt 5d orbital in Pt₃Ir alloy by reducing the ε_d energy level of Pt 5d

orbital to a deeper value, thus optimizing both the adsorption and desorption energies of H and H₂ and resulting in significantly improved HER activity. This work is expected to provide valuable insights into the development of self-supported electrodes with extraordinary HER performances under the guidance of the ε_d theory.

CRediT authorship contribution statement

Zhenrui Ni: Methodology, Data curation, Formal analysis, Writing-original draft. **Cheng Luo:** DFT Calculations, Data curation. **Bei Cheng** and **Youji Li:** Data curation, Funding acquisition, Software. **Panyong Kuang:** Formal analysis, Conceptualization, Writing-Reviewing and Editing. **Jiaguo Yu:** Supervision, Conceptualization, Writing-Reviewing and Editing.

Declaration of Competing Interest

The authors declare that they have no known competing financial interests or personal relationships that could have appeared to influence the work reported in this paper.

Data Availability

Data will be made available on request.

Acknowledgments

This work was supported by the National Key Research and Development Program of China (2018YFB1502001), National Natural Science Foundation of China (51932007, 51961135303, 22005232, 21871217, 21905219, 52073223, and U1905215), and China Postdoctoral Science Foundation (2022M712945, 2022T150598).

Appendix A. Supporting information

Supplementary data associated with this article can be found in the online version at doi:10.1016/j.apcatb.2022.122072.

References

- [1] Z. Zhou, Z. Pei, L. Wei, S. Zhao, X. Jian, Y. Chen, Electrocatalytic hydrogen evolution under neutral pH conditions: current understandings, recent advances, and future prospects, Energy Environ. Sci. 13 (2020) 3185–3206.
- [2] L. Zhang, Z. Wang, J. Qiu, Energy-saving hydrogen production by seawater electrolysis coupling sulfion degradation, Adv. Mater. 34 (2022) 2109321.
- [3] P. Kuang, Y. Wang, B. Zhu, F. Xia, C.W. Tung, J. Wu, H.M. Chen, J. Yu, Pt single atoms supported on N-doped mesoporous hollow carbon spheres with enhanced electrocatalytic H₂-evolution activity, Adv. Mater. 33 (2021) 2008599.
- [4] D. Gao, J. Xu, L. Wang, B. Zhu, H. Yu, J. Yu, Optimizing atomic hydrogen desorption of sulfur-rich NiS_{1+x} cocatalyst for boosting photocatalytic H₂ evolution, Adv. Mater. 34 (2022) 2108475.
- [5] J. Yu, A general route via carbon quantum dots assembled to prepare ruthenium based bimetallic electrocatalysts for pH-universal hydrogen evolution reaction, Acta Phys. Chim. Sin. 37 (2021) 2011004.
- [6] C. Tang, R. Zhang, W. Lu, Z. Wang, D. Liu, S. Hao, G. Du, A.M. Asiri, X. Sun, Energy-saving electrolytic hydrogen generation: Ni₂P nanoarray as a high-performance non-noble-metal electrocatalyst, Angew. Chem. Int. Ed. 56 (2017) 842–846.
- [7] F. Yu, H. Zhou, Y. Huang, J. Sun, F. Qin, J. Bao, W. Goddard, S. Chen, Z. Ren, High-performance bifunctional porous non-noble metal phosphide catalyst for overall water splitting, Nat. Commun. 9 (2018) 2551.
- [8] W. Hua, H. Sun, F. Xu, J. Wang, A review and perspective on molybdenum-based electrocatalysts for hydrogen evolution reaction, Rare Met. 39 (2020) 335–351.
- [9] M. Li, X. Zheng, L. Li, Z. Wei, Research progress of hydrogen oxidation and hydrogen evolution reaction mechanism in alkaline media, Acta Phys. -Chim. Sin. 37 (2021) 2007054.
- [10] P. Kuang, M. He, H. Zou, J. Yu, K. Fan, 0D/3D MoS₂-NiS₂/N-doped graphene foam composite for efficient overall water splitting, Appl. Catal. B Environ. 254 (2019) 15–25.
- [11] Y. Luo, Z. Zhang, M. Chhowalla, B. Liu, Recent advances in design of electrocatalysts for high-current-density water splitting, Adv. Mater. 34 (2022) 2108133.
- [12] C. Bie, L. Wang, J. Yu, Challenges for photocatalytic overall water splitting, Chem 8 (2022) 1567–1574.

[13] J. Zhu, L. Hu, P. Zhao, L.Y.S. Lee, K.Y. Wong, Recent advances in electrocatalytic hydrogen evolution using nanoparticles, *Chem. Rev.* 120 (2020) 851–918.

[14] X. Liu, Y. Deng, L. Zheng, M.R. Kesama, C. Tang, Y. Zhu, Engineering low-coordination single-atom cobalt on graphitic carbon nitride catalyst for hydrogen evolution, *ACS Catal.* 12 (2022) 5517–5526.

[15] Y. Tan, R. Xie, S. Zhao, X. Lu, L. Liu, F. Zhao, C. Li, H. Jiang, G. Chai, D. Brett, P. R. Shearing, G. He, I.P. Parkin, Facile fabrication of robust hydrogen evolution electrodes under high current densities via Pt@Cu interactions, *Adv. Funct. Mater.* 31 (2021) 2105579.

[16] X. Liu, R. Guo, K. Ni, F. Xia, C. Niu, B. Wen, J. Meng, P. Wu, J. Wu, X. Wu, L. Mai, Reconstruction-determined alkaline water electrolysis at industrial temperatures, *Adv. Mater.* 32 (2020) 2001136.

[17] H. Zhou, F. Yu, Q. Zhu, J. Sun, F. Qin, L. Yu, J. Bao, Y. Yu, S. Chen, Z. Ren, Water splitting by electrolysis at high current densities under 1.6 volts, *Energy Environ. Sci.* 11 (2018) 2858–2864.

[18] B. Zhang, L. Zhang, Q. Tan, J. Wang, J. Liu, H. Wan, L. Miao, J. Jiang, Simultaneous interfacial chemistry and inner Helmholtz plane regulation for superior alkaline hydrogen evolution, *Energy Environ. Sci.* 13 (2020) 3007–3013.

[19] Y. Liu, W. Li, H.B. Wu, S. Lu, Carbon dots enhance ruthenium nanoparticles for efficient hydrogen production in alkaline, *Acta Phys. -Chim. Sin.* 37 (2021) 2009082.

[20] H. Zou, B. He, P. Kuang, J. Yu, K. Fan, Ni_xS_y nanowalls/nitrogen-doped graphene foam is an efficient trifunctional catalyst for unassisted artificial photosynthesis, *Adv. Funct. Mater.* 28 (2018) 1706917.

[21] Z. Lei, W. Cai, Y. Rao, K. Wang, Y. Jiang, Y. Liu, X. Jin, J. Li, Z. Lv, S. Jiao, W. Zhang, P. Yan, S. Zhang, R. Cao, Coordination modulation of iridium single-atom catalyst maximizing water oxidation activity, *Nat. Commun.* 13 (2022) 24.

[22] R. Du, X. Jin, R. Hübner, X. Fan, Y. Hu, A. Eychmüller, Engineering self-supported noble metal foams toward electrocatalysis and beyond, *Adv. Energy Mater.* 10 (2019) 1901945.

[23] T. Dai, X. Zhang, M. Sun, B. Huang, N. Zhang, P. Da, R. Yang, Z. He, W. Wang, P. Xi, C.H. Yan, Uncovering the promotion of $\text{CeO}_2/\text{CoSi}_{1.97}$ heterostructure with specific spatial architectures on oxygen evolution reaction, *Adv. Mater.* 33 (2021) 2102593.

[24] Y. Wang, Y. Ding, C. Zhang, B. Xue, N. Li, L. Yu, Formation of hierarchical Co-decorated Mo_2C hollow spheres for enhanced hydrogen evolution, *Rare Met.* 40 (2021) 2785–2792.

[25] B. Zhong, P. Kuang, L. Wang, J. Yu, Hierarchical porous nickel supported NiFeO_xH_y nanosheets for efficient and robust oxygen evolution electrocatalyst under industrial condition, *Appl. Catal. B Environ.* 299 (2021), 120668.

[26] X. Liu, Y. Tian, F. Chen, A. Caratenuto, J. DeGiorgis, M. Elsonbaty, Y. Wan, R. Ahlgren, Y. Zheng, An easy-to-fabricate 2.5D evaporator for efficient solar desalination, *Adv. Funct. Mater.* 31 (2021) 2100911.

[27] L. Yu, L. Wu, B. McElhenny, S. Song, D. Luo, F. Zhang, Y. Yu, S. Chen, Z. Ren, Ultrafast room-temperature synthesis of porous S-doped Ni/Fe (oxy)hydroxide electrodes for oxygen evolution catalysis in seawater splitting, *Energy Environ. Sci.* 13 (2020) 3439–3446.

[28] T. Kou, S. Wang, R. Shi, T. Zhang, S. Chiavoloni, J.Q. Lu, W. Chen, M.A. Worsley, B. C. Wood, S.E. Baker, E.B. Duoss, R. Wu, C. Zhu, Y. Li, Periodic porous 3d electrodes mitigate gas bubble traffic during alkaline water electrolysis at high current densities, *Adv. Energy Mater.* 10 (2020) 2002955.

[29] L. Hui, Y. Xue, D. Jia, H. Yu, C. Zhang, Y. Li, Multifunctional single-crystallized carbonate hydroxides as highly efficient electrocatalyst for full water splitting, *Adv. Energy Mater.* 8 (2018) 1800175.

[30] S. Anantharaj, T.S. Amarnath, E. Subashini, S. Chatterjee, K.C. Swaathini, K. Karthick, S. Kundu, Shrinking the hydrogen overpotential of Cu by 1 V and imparting ultralow charge transfer resistance for enhanced H_2 evolution, *ACS Catal.* 8 (2018) 5686.

[31] G. Nagaraju, S.C. Sekhar, B. Ramulu, J.S. Yu, High-performance hybrid supercapacitors based on MOF-derived hollow ternary chalcogenides, *Energy Stor. Mater.* 35 (2021) 750.

[32] Y. Wang, R. Li, H. Li, H. Huang, Z. Guo, H. Chen, Y. Zheng, K. Qu, Controlled synthesis of ultrasmall RuP_2 particles on N,P-codoped carbon as superior pH-wide electrocatalyst for hydrogen evolution, *Rare Met.* 40 (2021) 1040–1047.

[33] F. Zhou, Y. Zhou, G. Liu, C. Wang, J. Wang, Recent advances in nanostructured electrocatalysts for hydrogen evolution reaction, *Rare Met.* 40 (2021) 3375–3405.

[34] X. Yu, Z.Y. Yu, X.L. Zhang, Y.R. Zheng, Y. Duan, Q. Gao, R. Wu, B. Sun, M.R. Gao, G. Wang, S.H. Yu, "Superaerophobic" nickel phosphide nanoarray catalyst for efficient hydrogen evolution at ultrahigh current densities, *J. Am. Chem. Soc.* 141 (2019) 7537–7543.

[35] Q. Wen, K. Yang, D. Huang, G. Cheng, X. Ai, Y. Liu, J. Fang, H. Li, L. Yu, T. Zhai, Schottky heterojunction nanosheet array achieving high-current-density oxygen evolution for industrial water splitting electrolyzers, *Adv. Energy Mater.* 11 (2021) 2102353.

[36] Q. Che, Q. Li, Y. Tan, X. Chen, X. Xu, Y. Chen, One-step controllable synthesis of amorphous $(\text{Ni}-\text{Fe})\text{S}_x/\text{NiFe}(\text{OH})$ hollow microtube/sphere films as superior bifunctional electrocatalysts for quasi-industrial water splitting at large-current-density, *Appl. Catal. B: Environ.* 246 (2019) 337–348.

[37] H. Wang, T. Zhou, P. Li, Z. Cao, W. Xi, Y. Zhao, Y. Ding, Self-supported hierarchical nanostructured NiFe-LDH and Cu_3P weaving mesh electrodes for efficient water splitting, *ACS Sustain. Chem. Eng.* 6 (2017) 380–388.

[38] P. Kuang, M. Sayed, J. Fan, B. Cheng, J. Yu, 3D graphene-based H_2 -production photocatalyst and electrocatalyst, *Adv. Energy Mater.* 10 (2020) 1903802.

[39] H. Yang, M. Driess, P.W. Menezes, Self-supported electrocatalysts for practical water electrolysis, *Adv. Energy Mater.* 11 (2021) 2102074.

[40] J. Feng, H. Xu, Y. Dong, S. Ye, Y. Tong, G. Li, FeOOH/Co/FeOOH hybrid nanotube arrays as high-performance electrocatalysts for the oxygen evolution reaction, *Angew. Chem. Int. Ed.* 55 (2016) 3694–3698.

[41] H. Yang, Z. Chen, P. Guo, B. Fei, R. Wu, B-doping-induced amorphization of LDH for large-current-density hydrogen evolution reaction, *Appl. Catal. B: Environ.* 261 (2020), 118240.

[42] L. Yu, H. Zhou, J. Sun, F. Qin, F. Yu, J. Bao, Y. Yu, S. Chen, Z. Ren, Cu nanowires shelled with NiFe layered double hydroxide nanosheets as bifunctional electrocatalysts for overall water splitting, *Energy Environ. Sci.* 10 (2017) 1820–1827.

[43] W. Chen, B. Wu, Y. Wang, W. Zhou, Y. Li, T. Liu, C. Xie, L. Xu, S. Du, M. Song, D. Wang, Y. liu, Y. Li, J. Liu, Y. Zou, R. Chen, C. Chen, J. Zheng, Y. Li, J. Chen, S. Wang, Deciphering the alternating synergy between interlayer Pt single-atom and NiFe layered double hydroxide for overall water splitting, *Energy Environ. Sci.* 14 (2021) 6428.

[44] X. Li, L. Zheng, S. Liu, T. Ouyang, S. Ye, Z. Liu, Heterostructures of NiFe LDH hierarchically assembled on MoS_2 nanosheets as high-efficiency electrocatalysts for overall water splitting, *Chin. Chem. Lett.* 33 (2022) 4761–4765.

[45] H. Su, J. Jiang, N. Li, Y. Gao, L. Ge, NiCu alloys anchored defect-rich NiFe layered double-hydroxides as efficient electrocatalysts for overall water splitting, *Chem. Eng. J.* 446 (2022), 137226.

[46] W. Xu, Z. Lu, P. Wan, Y. Kuang, X. Sun, High-performance water electrolysis system with double nanostructured superaerophobic electrodes, *Small* 12 (2016) 2492–2498.

[47] Z. Li, H. Jiang, D. Qin, X. Jiang, X. Ji, M.G. Kim, L. Zhang, X. Liu, J. Cho, Alloy-strain-output induced lattice dislocation in $\text{Ni}_3\text{FeN}/\text{Ni}_3\text{Fe}$ ultrathin nanosheets for highly efficient overall water splitting, *J. Mater. Chem. A* 9 (2021) 4036–4043.

[48] C. Cai, K. Liu, Y. Zhu, P. Li, Q. Wang, B. Liu, S. Chen, H. Li, L. Zhu, H. Li, J. Fu, Y. Chen, E. Pensa, J. Hu, Y.R. Lu, T.S. Chan, E. Cortes, M. Liu, Optimizing Hydrogen binding on Ru sites with RuCo alloy nanosheets for efficient alkaline hydrogen evolution, *Angew. Chem. Int. Ed.* 61 (2022) 202113664.

[49] J. Wang, S. Xin, Y. Xiao, Z. Zhang, Z. Li, W. Zhang, C. Li, R. Bao, J. Peng, J. Yi, S. Chou, Manipulating the water dissociation electrocatalytic sites of bimetallic Ni-based alloy for highly-efficient alkaline hydrogen evolution, *Angew. Chem. Int. Ed.* (2022), e202202518.

[50] Q. Xia, D. Zhang, Z. Yao, Z. Jiang, Investigation of Cu heteroatoms and Cu clusters in Fe-Cu alloy and their special effect mechanisms on the Fenton-like catalytic activity and reusability, *Appl. Catal. B Environ.* 299 (2021), 120662.

[51] P. Kuang, M. He, B. Zhu, J. Yu, K. Fan, M. Jaroniec, 0D/2D $\text{NiS}_2/\text{V-MXene}$ composite for electrocatalytic H_2 evolution, *J. Catal.* 375 (2019) 8–20.

[52] R. Li, P. Kuang, L. Wang, H. Tang, J. Yu, Engineering 2D $\text{NiO}/\text{Ni}_3\text{S}_2$ heterointerface electrocatalyst for highly efficient hydrogen production coupled with benzyl alcohol oxidation, *Chem. Eng. J.* 431 (2022), 134137.

[53] P. Kuang, B. Zhu, Y. Li, H. Liu, J. Yu, K. Fan, Graphdiyne: a superior carbon additive to boost the activity of water oxidation catalysts, *Nanoscale Horiz.* 3 (2018) 317–326.

[54] W. Zhao, H. Xu, H. Luan, N. Chen, P. Gong, K. Yao, Y. Shen, Y. Shao, NiFe layered double hydroxides grown on a corrosion-cell cathode for oxygen evolution electrocatalysis, *Adv. Energy Mater.* 12 (2021) 2102372.

[55] J. Chen, Q. Long, K. Xiao, T. Ouyang, N. Li, S. Ye, Z. Liu, Vertically-interlaced $\text{NiFeP}/\text{MXene}$ electrocatalyst with tunable electronic structure for high-efficiency oxygen evolution reaction, *Sci. Bull.* 66 (2021) 1063–1072.

[56] W. Zhao, C. Luo, Y. Lin, G. Wang, H.M. Chen, P. Kuang, J. Yu, Pt–Ru dimer electrocatalyst with electron redistribution for hydrogen evolution reaction, *ACS Catal.* 12 (2022) 5540–5548.

[57] Y. Wang, B. Zhu, B. Cheng, W. Macyk, P. Kuang, J. Yu, Hollow carbon sphere-supported Pt/Co hybrid with excellent hydrogen evolution activity and stability in acidic environment, *Appl. Catal. B Environ.* 314 (2022), 121503.

[58] L. Yu, I.K. Mishra, Y. Xie, H. Zhou, J. Sun, J. Zhou, Y. Ni, D. Luo, F. Yu, Y. Yu, S. Chen, Z. Ren, Ternary $\text{Ni}_{2(1-x)}\text{Mo}_{2x}\text{P}$ nanowire arrays toward efficient and stable hydrogen evolution electrocatalysis under large-current-density, *Nano Energy* 53 (2018) 492–500.

[59] Y. Rao, S. Wang, R. Zhang, S. Jiang, S. Chen, Y. Yu, S. Bao, M. Xu, Q. Yue, H. Xin, Y. Kang, Nanoporous V-doped Ni_3P_4 microsphere: a highly efficient electrocatalyst for hydrogen evolution reaction at All pH, *ACS Appl. Mater. Interfaces* 12 (2020) 37092–37099.

[60] Y. Wang, G. Qian, Q. Xu, H. Zhang, F. Shen, L. Luo, S. Yin, Industrially promising IrNi-FeNi_3 hybrid nanosheets for overall water splitting catalysis at large current density, *Appl. Catal. B Environ.* 286 (2021), 119881.

[61] J. Yang, A.R. Mohmad, Y. Wang, R. Fullon, X. Song, F. Zhao, I. Bozkurt, M. Augustina, E.J.G. Santos, H.S. Shin, W. Zhang, D. Voiry, H.Y. Jeong, M. Chhowalla, Ultrahigh-current-density niobium disulfide catalysts for hydrogen evolution, *Nat. Mater.* 18 (2019) 1309–1314.

[62] X. Zhang, F. Li, R. Fan, J. Zhao, B. Dong, F. Wang, H. Liu, J. Yu, C. Liu, Y. Chai, F. P double-doped Fe_3O_4 with abundant defect sites for efficient hydrogen evolution at high current density, *J. Mater. Chem. A* 9 (2021) 15836–15845.

[63] P.W. Menezes, A. Indra, I. Zaharieva, C. Walter, S. Loos, S. Hoffmann, R. Schlögl, H. Dau, M. Driess, Helical cobalt borophosphates to master durable overall water-splitting, *Energy Environ. Sci.* 12 (2019) 988–999.

[64] G. Zhang, A. Wang, L. Niu, W. Gao, W. Hu, Z. Liu, R. Wang, J. Chen, Interfacial engineering to construct antioxidative $\text{Pd}_4\text{S}/\text{Pd}_3\text{P}_{0.95}$ heterostructure for robust hydrogen production at high current density, *Adv. Energy Mater.* 12 (2022) 2103511.

[65] C. Zhang, Y. Luo, J. Tan, Q. Yu, F. Yang, Z. Zhang, L. Yang, H.M. Cheng, B. Liu, High-throughput production of cheap mineral-based two-dimensional

electrocatalysts for high-current-density hydrogen evolution, *Nat. Commun.* 11 (2020) 3724.

[66] P. Kuang, L. Zhang, B. Cheng, J. Yu, Enhanced charge transfer kinetics of $\text{Fe}_2\text{O}_3/\text{CdS}$ composite nanorod arrays using cobalt-phosphate as cocatalyst, *Appl. Catal. B Environ.* 218 (2017) 570–580.

[67] F. Malara, A. Minguzzi, M. Marelli, S. Morandi, R. Psaro, V. Dal Santo, A. Naldoni, $\alpha\text{-Fe}_2\text{O}_3/\text{NiOOH}$: an effective heterostructure for photoelectrochemical water oxidation, *ACS Catal.* 5 (2015) 5292–5300.

[68] S. Sun, X. Zhou, B. Cong, W. Hong, G. Chen, Tailoring the d-Band centers endows $(\text{Ni}_x\text{Fe}_{1-x})_2\text{P}$ nanosheets with efficient oxygen evolution catalysis, *ACS Catal.* 10 (2020) 9086–9097.

[69] J. Yan, L. Kong, Y. Ji, J. White, Y. Li, J. Zhang, P. An, S. Liu, S.T. Lee, T. Ma, Single atom tungsten doped ultrathin alpha- $\text{Ni}(\text{OH})_2$ for enhanced electrocatalytic water oxidation, *Nat. Commun.* 10 (2019) 2149.